Advanced Engineering Informatics 69 (2026) 103992

Contents lists available at ScienceDirect

Advanced Engineering Informatics

journal homepage: www.elsevier.com/locate/aei

Full length article

Real-time deformation digital twin of composite plates via distributed fiber optic sensing

Yingwu Li [a], Yuhang Pan [b],*, Zahra Sharif-Khodaei [b]

[a] Beijing Institute of Technology, Haidian, Beijing, 100081, China
[b] Imperial College London, Exhibition Road, London, SW7 2AZ, United Kingdom

ARTICLE INFO

Keywords:
Dynamic shape reconstruction
Digital twin
Deformation detection
Distributed fiber optic sensing
Inverse finite element method

ABSTRACT

Dynamic shape reconstruction is critical for developing high-fidelity digital twin of structures, enabling early detection of large deformations and hence optimizing structural design and operation. To address challenges such as time-synchronized data acquisition, environmental and operational variations (EOVs), and dynamic validation and calibration, this study proposes a novel deformation digital twin framework for precise dynamic shape reconstruction of composite structures. The framework integrates 1D distributed fiber optic sensing for high-resolution strain acquisition, the inverse finite element method for shape reconstruction, and synchronized motion capture for dynamic validation. Experiments conducted on composite structures subjected to sinusoidal vibration loads at varying frequencies (5 Hz, 8 Hz, 10 Hz, and 15 Hz) and positions demonstrated a maximum displacement error below 0.3 mm, verifying the framework's precision and robustness. Key contributions include the optimized digital representation of the fiber optic sensor network, high-fidelity reconstruction of dynamic deformations, and validation using a real-time motion capture system. These advancements offer a novel approach to structural digital twins, facilitating predictive maintenance, optimizing design and operation, and enhancing safety. This paves the way for sustainable and advanced industrial applications, particularly in aerospace and other engineering fields that demand precise shape sensing under EOVs.

1. Introduction

Dynamic shape reconstruction is essential in various industrial fields, including aerospace [1], manufacturing [2,3], and civil engineering [4,5]. In aerospace, for instance, shape information provides critical data for optimizing structural parameters, thereby improving product performance and durability [6] and optimizing its service life. Throughout the service lifespan of structures, shape-based structural health monitoring (SHM) allows for the early detection of potential damage, enabling intelligent maintenance strategies [7]. This not only significantly reduces the high costs of regular maintenance but also effectively extends the lifespan of structures [8]. As such, shape reconstruction technology has gained significant attention in recent years, particularly in the design and health monitoring of structures, becoming a focal point of extensive research effort.

Non-contact measurement techniques, such as laser scanning [9,10] and digital image correlation [11], are among the most direct approaches for shape reconstruction. Despite their capability to achieve high accuracy, these methods are often constrained to localized measurements in real-time applications or limited in capturing full-field deformations of complex structures. Consequently, their competitiveness in real-time shape reconstruction is reduced [12,13]. Numerical simulations, such as finite element methods [14,15], demonstrate excellent performance in predicting structural shapes under determined loads. However, their practical implementation faces considerable challenges due to the complexity of loading conditions, boundary constraints, and uncertainties in material parameters, such as Young's modulus and Poisson's ratio [16].

Building on this foundation, strain-based shape reconstruction has become the widely used approach for real-world applications, supported by the availability of lightweight and accurate strain acquisition systems [17]. These methods can be broadly categorized into three groups: numerical integration methods [18,19], basis function approximation methods [20,21], and inverse finite element methods (iFEM) [22]. Among these, iFEM stands out as one of the most promising techniques [17,23]. By inversely computing the displacement field from limited strain measurement data, iFEM achieves high reconstruction accuracy even with sparse data and demonstrates strong robustness against measurement noise [24,25].

The iFEM, initially introduced by Alexander Tessler and Jan L. Spangler, was designed to solve the shape reconstruction problem in

* Corresponding author.
E-mail address: y.pan21@imperial.ac.uk (Y. Pan).

https://doi.org/10.1016/j.aei.2025.103992
Received 7 July 2025; Received in revised form 2 October 2025; Accepted 15 October 2025
Available online 21 October 2025

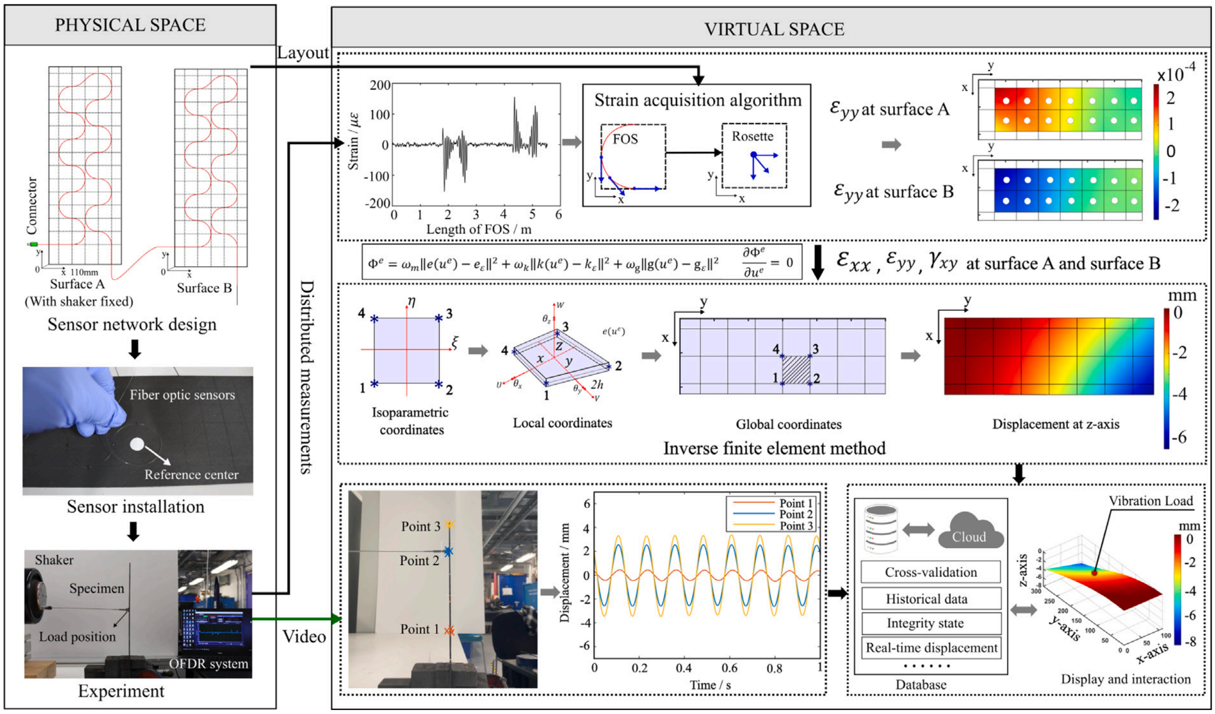

Fig. 1. The digital twin model proposed in this research for deformation reconstruction.

shell structures using first-order deformation theory [26]. The core principle of iFEM involves minimizing the discrepancy between measured and predicted strains through finite element discretization and a least-squares variational approach, enabling the computation of the displacement field. Building on this framework, researchers have extended iFEM to various structural applications under different kinematic assumptions, including ship hulls [27], wind turbines [28,29], subsea pipelines [30], and tunnel monitoring systems [31,32]. Despite its potential, dynamic shape reconstruction using iFEM has received limited attention, primarily due to the inherent challenges associated with sensor integration, data processing, environmental and operational variations (EOVs), and dynamic validation and calibration. For example, high-accuracy shape reconstruction necessitates time-synchronized data acquisition from an optimized sensor network [33]. Furthermore, the development of a sensor network that is robust against EOVs and the implementation of a reliable dynamic validation framework are critical for ensuring the reliability and accuracy of the reconstructed results [34].

Digital twin (DT) technology [35,36], which enables seamless integration between physical and virtual systems, represents a promising approach to address the challenges of dynamic shape reconstruction using iFEM. First, DT inherently relies on time-synchronized strain measurements, as it emphasizes bidirectional and real-time data exchange between the physical and digital domains [37,38]. Second, DT facilitates the integration of EOV parameters, iFEM-based shape reconstruction algorithms, and dynamic validation procedures within a continuously updating digital framework [39,40]. Finally, the incorporation of advanced statistical and machine learning algorithms within DT frameworks holds considerable potential to further enhance reconstruction accuracy [41]. Beyond real-time monitoring, the application of DT can be systematically classified into two complementary phases: design and operation. In the design phase, DT models enable rapid validation and iterative testing, thereby identifying sources of inefficiency early in the system development process. Recent studies have emphasized DT as a key enabler of manufacturing system design during the transition from Industry 4.0 to Industry 5.0, supporting virtual commissioning and optimization prior to physical implementation [42,43]. In the operation phase, DT acts as a closed-loop feedback mechanism, continuously issuing adjustment instructions to the physical system to improve performance and resilience. This capability has been demonstrated in DT-enabled remote semi-physical commissioning of flow-type manufacturing systems and in blockchain-based smart contract frameworks that support decentralized autonomous manufacturing [44,45]. Leveraging a similar design–operation integration paradigm for iFEM-based dynamic shape reconstruction could significantly improve scalability, robustness, and the practical relevance of structural health monitoring systems in real-world applications [46,47]. Beyond engineering structures, the proposed framework could also be extended to human digital twin (HDT) systems, where accurate and real-time deformation reconstruction is crucial for applications such as personalized healthcare and rehabilitation [48–50]

This study aims to address the challenges in dynamic shape reconstruction using iFEM by introducing a real time deformation DT framework that integrates a strain acquisition scheme based on distributed fiber optic sensing [51], iFEM, and dynamic validation using motion capture. To achieve time-synchronized strain measurements while mitigating the effects of EOVs, a strain acquisition scheme leveraging distributed fiber optic sensing is proposed. This scheme emphasizes the digital representation of the sensor network and adaptive updates of strain data to accommodate operational variations, such as adjustments to the iFEM mesh or sensor layout. Additionally, the inherent robustness of fiber optic sensors to harsh operating conditions, including corrosion, electromagnetic interference, and extreme temperatures, further enhances the resilience to EOVs of the proposed scheme. For dynamic validation and calibration, a motion capture approach based on the Kanade–Lucas–Tomasi (KLT) algorithm is employed, providing a low-cost, flexible, and easily implemented solution. The proposed DT framework demonstrates high reliability, accuracy, and practicality in dynamic shape reconstruction for critical structures, as validated through experimental studies on composite structures in this work. The key contributions are summarized as follows:

- A novel DT framework is proposed to facilitate dynamic shape reconstruction with high reliability and accuracy by integrating a real-time strain acquisition scheme, the iFEM, and a dynamic validation mechanism. The framework predicts the full deformation

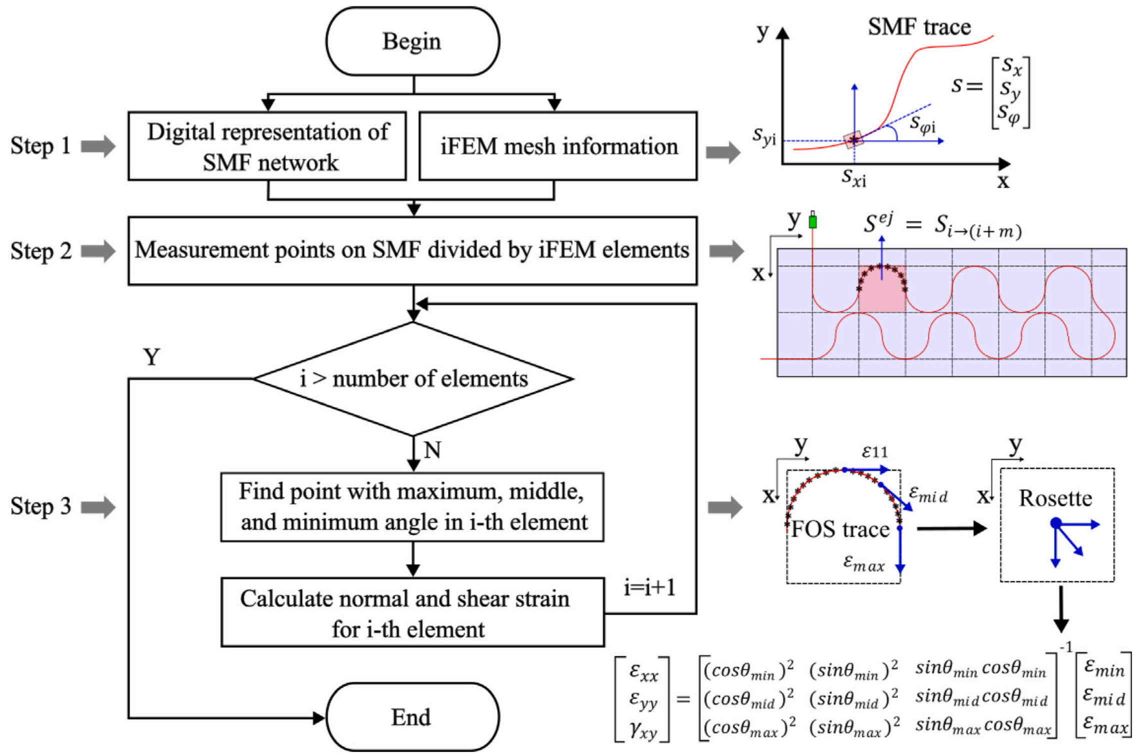

Fig. 2. The flow diagram of proposed strain acquisition algorithm.

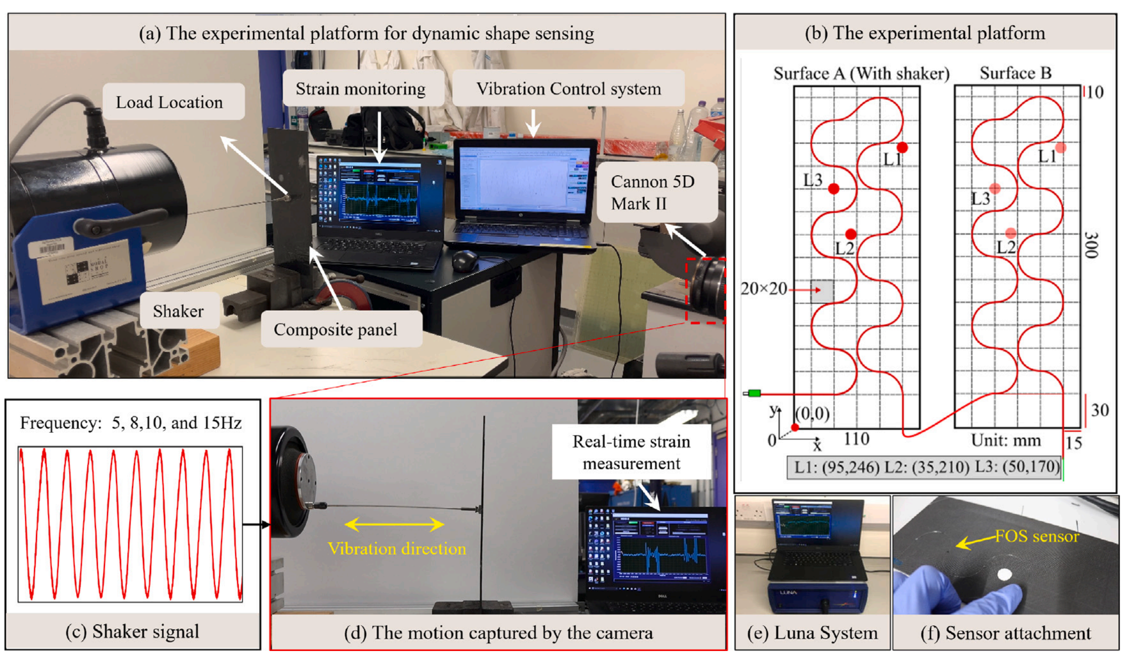

Fig. 3. The experimental platform for deformation reconstruction: (a) the overall experimental set-up; (b) the layout of the Fiber optical sensors; (c) the signal used for shaker (Frequencies are 5, 8, 10, 15 Hz); (d) the specimen motion captured by the camera and the real-time strain measurement; (e) Luna system for the strain measurement; (f) the sensor attachment process.

field of composite plates based on 1D strain reading along a fiber optic sensors.

- A real-time strain acquisition scheme leveraging distributed fiber optic sensing is developed, offering advantages in digitalization, adaptive updating, and mitigation of EOVs.
- Dynamic shape reconstruction of composite plate under various vibration modes, characterized by differing frequencies and load positions, is successfully achieved using the iFEM.
- A dynamic validation and calibration mechanism based on the KLT algorithm is introduced, demonstrating high accuracy in dynamic shape reconstruction results.

The paper is structured as follows: Section 2 outlines the proposed methodology, including the proposed DT framework, the strain acquisition scheme, the iFEM approach, and the KLT algorithm. Section 3 provides details of the experimental setup, including the configuration

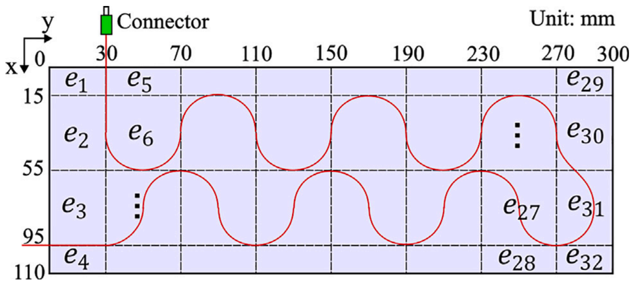

Fig. 4. The iFEM mesh utilized in this study.

of fiber optic sensors, the shaker system, the specimen motion capture system, and the sensor installation process. Section 4 discusses the results of strain acquisition, shape reconstruction, motion capture, and error analysis. Finally, the key conclusions of this study are summarized in Section 5.

2. Methodology

This section begins with an overview of the proposed real-time deformation DT framework, followed by a detailed presentation of the main methodologies employed within the framework. These include the dynamic strain acquisition scheme (Section 2.2), the iFEM (Section 2.3), and the KLT algorithm (Section 2.4).

2.1. Deformation digital twin framework

The DT model proposed in this research is presented in Fig. 1, which illustrates the physical domain and data flow within the system. The physical domain includes the design of the sensor network, the installation of single-mode fiber (SMF), and the execution of vibration experiments. Three types of data are generated for deformation reconstruction and validation. First, the digital representation of the sensor network layout provides the spatial framework for data integration. Second, strain measurements from the Optical Frequency Domain Reflectometry (OFDR) system complement this layout by capturing strain information along the axis of SMF. These measurements must be transformed before being applied in iFEM calculations. Third, videos recorded during the vibration experiments serve as a reference for validating the deformation results obtained through iFEM, ensuring the reliability of the reconstructed shapes. To synchronize the OFDR measurements (100 Hz in this work) and the validation camera (60 Hz in this work), the entire system is triggered simultaneously to share a common starting reference. During post-processing, both data streams are aligned over constant time intervals, and error analysis is performed at common sampling instants (e.g., 20 Hz by matching corresponding frames and OFDR samples). The analysis frequency can be further down-sampled (e.g., to 10 Hz or 1 Hz) to reduce computational burden, without introducing noticeable time-alignment error. Fig. 1 integrates these components, highlighting their roles in creating an accurate and robust DT model.

The virtual space of this DT model consists of four key components [52]. The first component is the strain acquisition algorithm, which calculates normal and shear strains on the surfaces of the carbon-fiber reinforced polymer (CFRP) specimen based on axial strain data obtained from OFDR system. The second component focuses on deformation reconstruction using the iFEM method, serving as the core of the DT model. The third component involves tracking the displacement variation of the CFRP specimen during experiments through motion capture from recorded videos. The fourth component encompasses result validation, data storage, and visualization. Real-time deformation validation is achieved by comparing iFEM outputs with motion capture data. Additionally, a structured database integrates local and cloud storage, supporting functions such as historical data retrieval, integrity state assessments, and real-time deformation visualization. Collectively, these components establish a robust virtual space that enables precise deformation monitoring and comprehensive structural assessments. Detailed descriptions of the techniques employed, including OFDR, the strain acquisition algorithm, iFEM, and the motion capture algorithm, are provided in the following subsections.

2.2. Dynamic strain acquisition scheme based on distributed fiber optic sensing

OFDR is a highly accurate technique for measuring parameters such as strain and temperature in a distributed manner. With advantages such as lightweight design, resistance to electromagnetic interference, high-temperature stability, and corrosion resistance, OFDR demonstrates significant potential for SHM in aircraft applications. The fundamental principle of OFDR is based on the frequency shift of Rayleigh backscattering in SMF subjected to thermal and mechanical loads [53,54]. This principle is mathematically described as:

$$\Delta \upsilon = K_T \Delta T + K_\varepsilon \Delta \varepsilon \tag{1}$$

In this equation, $\Delta \upsilon$ represents the frequency shift of Rayleigh backscattering in SMF, ΔT denotes the thermal load, and $\Delta \varepsilon$ indicates the mechanical load. According to related research, the frequency shifts caused by thermal and mechanical loads in OFDR are both linear with respect to their variables and mutually independent, meaning that temperature and strain contribute separately to the total frequency shift without any coupling [55]. Therefore, both the temperature-frequency shift coefficient (K_T) and the strain-frequency shift coefficient (K_ε) are constants. Detailed expressions for these two coefficients can be found in [56].

As mentioned in Section 2.1, the strain data obtained by the OFDR system only provides strain information along the axis direction of the SMF. Therefore, this research proposes an algorithm to convert the OFDR measurements into normal and shear strains on both surfaces of the CFRP specimen. The flow diagram of the proposed algorithm is illustrated in Fig. 2.

As shown in Fig. 2, the algorithm is divided into three steps. In the first step, the designed SMF network is represented numerically by a matrix S. This matrix contains the coordinates and measurement directions of each measurement segment on the fiber optic sensors. The structure of the matrix is expressed in Eq. (2) as follows:

$$S = \begin{bmatrix} S_x \\ S_y \\ S_\varphi \end{bmatrix} = \begin{bmatrix} S_{x1} & S_{x2} & \cdots & S_{xi} & \cdots & S_{xn} \\ S_{y1} & S_{y2} & \cdots & S_{yi} & \cdots & S_{yn} \\ S_{\varphi 1} & S_{\varphi 1} & \cdots & S_{\varphi i} & \cdots & S_{\varphi n} \end{bmatrix} \tag{2}$$

where n is the total number of measurement segments. The information for the ith measurement segment is represented by S_{xi}, S_{yi}, and $S_{\phi i}$, which correspond to the x-coordinate, y-coordinate, and measurement direction, respectively.

In the second step, the mesh information of iFEM is integrated into the digital representation of the SMF network. Specifically, since the coordinates of all measurement segments are available in S, those measurement segments within jth iFEM element can be further packaged into a sub-matrix S^{ej} according to the mesh information. Therefore, the matrix S is transformed to a final digital representation of SMF network (S^e) as follows:

$$S^e = \begin{bmatrix} S^{e1} & S^{e2} & \dots & S^{ej} & \dots & S^{ek} \end{bmatrix} \tag{3}$$

where $[S^{ej}]$ denotes a sub-matrix containing the measurement segments within the jth iFEM element, and k represents the total number of iFEM elements. When the number of measurement segments within the k iFEM elements is defined as $n_1, n_2, \dots, n_j, \dots, n_k$, the total number of measurement segments is expressed as $n = n_1 + n_2 + \cdots + n_j + \cdots + n_k$. The digital representation of the SMF network, derived from the first and second steps, is established once during the initialization phase of the DT framework. Subsequent updates are triggered by events such as modifications to the sensor network or iFEM mesh, which can enhance the efficiency of real-time computing.

In the third step, the normal and shear strains of each iFEM element are calculated using the strain rosette principle. This calculation is based on the digital representation of the sensor network and the strain measurements from the OFDR system. Specifically, three segments within an iFEM element (e.g., S^{ej}) are selected to function as three “strain gauges”. These three segments are chosen to maximize their angular difference for higher stability according to the strain rosette principle. This process is expressed as:

$$\begin{bmatrix}\varepsilon_{xx}\\ \varepsilon_{yy}\\ \gamma_{xy}\end{bmatrix}=\begin{bmatrix}(cos\theta_1)^2 & (sin\theta_1)^2 & sin\theta_1 cos\theta_1\\ (cos\theta_2)^2 & (sin\theta_2)^2 & sin\theta_2 cos\theta_2\\ (cos\theta_3)^2 & (sin\theta_3)^2 & sin\theta_3 cos\theta_3\end{bmatrix}^{-1}\begin{bmatrix}\varepsilon_1\\ \varepsilon_2\\ \varepsilon_3\end{bmatrix} \tag{4}$$

where ε_{xx} and ε_{yy} represent the normal strains of an iFEM element, while γ_{xy} denotes the shear strain. The variables θ_1, θ_2, and θ_3 correspond to the measurement angles of the three selected segments within the iFEM element, respectively. The strain measurements obtained from the OFDR system for these three segments are denoted as ε_1, ε_2, and ε_3. As a result, the normal and shear strains can be dynamically updated with the continuous output from the OFDR system.

It is important to note that, unlike a traditional strain rosette composed of colocated strain gauges, the three measurement segments of the proposed “equivalent strain rosette” are generally not positioned at the same in-plane location within the iFEM element. This non-colocation may introduce errors, especially in extreme cases where the strain field exhibits strong gradients. However, under the iFEM formulation, the strain distribution within each element is assumed to be uniform, and only a representative strain value is required for the calculations rather than a complete strain field [27]. Consequently, the discrepancy introduced by the “equivalent strain rosette” is of the same order as the intrinsic approximation error of iFEM itself and therefore negligible. In fact, if the difference between a colocated strain rosette and the proposed equivalent (non-colocated) rosette were significant, it would imply that the uniform strain assumption of iFEM has already broken down, regardless of the sensor type. To further reduce such approximation errors, one can refine the mesh and increase the sensor density, albeit at the cost of higher measurement requirements.

2.3. iFEM

The shape reconstruction of composite laminates in this research is performed using the iFEM with drilling degrees of freedom [27]. This method estimates the displacement field of shell structures by comparing numerically interpolated strains with experimentally measured strains, utilizing a least-squares functional. For each element in the iFEM mesh, the least-squares functional is expressed as:

$$\Phi^e = \omega_m\|e(u^e)-e_\varepsilon\|^2+\omega_k\|k(u^e)-k_\varepsilon\|^2+\omega_g\|g(u^e)-g(\varepsilon)\|^2 \tag{5}$$

In this equation, u^e represents the estimated nodal displacement of an iFEM element. The terms $e(u^e)$, $k(u^e)$, and $g(u^e)$ correspond to the membrane, bending, and transverse components of the estimated strain field associated with u^e, respectively. These components can be computed using experimental strain data, denoted as e_ε, k_ε, and g_ε. The constant coefficients ω_m, ω_k, and ω_g are introduced to adjust the contributions of the membrane, bending, and transverse components in the functional, particularly for elements where strain data is unavailable. According to relevant literature [27], the values of these coefficients are typically set to less than 10^{-5} for an iFEM element when experimental strain data is absent. For detailed expressions of the parameters, including u^e, $e(u^e)$, $k(u^e)$, $g(u^e)$, e_ε, k_ε, and g_ε, readers are referred to [27]. Based on this formulation, the nodal displacement (u^e) is determined by minimizing the least-squares functional, which is mathematically expressed as:

$$\frac{\partial\Phi^e}{\partial u^e}=k^e u^e-f^e=0 \tag{6}$$

In this equation, k^e is a constant coefficient matrix associated with the nodal displacement vector u^e, which is determined by the iFEM mesh and numerical interpolation. The vector f^e represents the strain data, including both normal and shear strains, calculated from experimental measurements. Detailed expressions for k^e and f^e can be found in [8]. After assembling all the elements, the displacement field of the structure U can be obtained using the following equation:

$$KU=F \tag{7}$$

where $K=\sum k^e$, $U=\sum u^e$, and $F=\sum f^e$ (the summation symbol $\sum$ represents the assembly process of the n iFEM elements). Similar to the digital representation (S^e) of the SMF network, the coefficient matrix of the structure (K) only needs to be established once during the initialization phase of the DT framework, unless the iFEM mesh is modified during operation. This configuration significantly enhances the efficiency of real-time computations.

2.4. Motion capture based on KLT algorithm

The KTL algorithm is a motion capture technique that has been extensively validated and widely implemented in real-world applications [57–59]. In this study, the KLT algorithm is employed as a low-cost, flexible, and easy-to-implement solution for the dynamic validation of shape reconstruction results within the proposed DT framework. This algorithm tracks the motion of target objects by analyzing pixel matrices that contain rich spatial intensity information in images. Specifically, let $I(x,y)$ represent the pixel matrix of interest in image W. After motion, this pixel matrix is transformed to $J(x',y')$. The displacement is represented by $d=[d_x,d_y]^T$. Consequently, the residual error between I and J can be mathematically expressed as :

$$\epsilon=\iint_W\left\|J\left(x+\frac{d_x}{2},y+\frac{d_y}{2}\right)-I\left(x-\frac{d_x}{2},y-\frac{d_y}{2}\right)\right\|^2dxdy \tag{8}$$

Therefore, this residual error is minimized to determine the displacement between I and J, as expressed in Eq. (9).

$$\frac{\partial\epsilon}{\partial d}=Gd-e=0 \tag{9}$$

In this equation, G and e are coefficient matrices with dimensions 2×2 and 2×1, respectively. For the complete derivation and expressions of these two matrices, please refer to the relevant literature in [60]. In this study, the motion capture process is automated using the Computer Vision Toolbox in MATLAB.

3. Experiments

To validate the proposed deformation DT, a series of experiments were designed and conducted. The experimental setup is summarized in Fig. 3. A composite structure, composed of 12 layers of M21-TS800 prepreg plies arranged in the sequence [+45/−45/0/90/0]s, was chosen as the structure for dynamic shape reconstruction. As shown in Fig. 3(a), the experimental platform consists of the specimen with the SMF network, a vibration generation system, a distributed fiber optic sensing system, and an optical imaging system.

The specimen with the SMF network is described in Fig. 3(b), which provides details on the specimen's dimensions, the geometric distribution of the SMF network, and the vibration load positions. The specimen's dimensions are 300 mm × 110 mm × 2 mm. The SMF network was designed and installed following the procedure outlined in our previous work [61]. Specifically, the SMF is naturally bent into a series of semicircles with a radius of 20 mm and bonded to both surfaces of the specimen using epoxy. This layout facilitates the implementation of the proposed “equivalent strain rosette” and follows the fiber's natural bending path, which can be modeled using Euler's elastica theory for accurate digital representation of the sensing network. Moreover, the natural bending strategy is easy to implement experimentally without

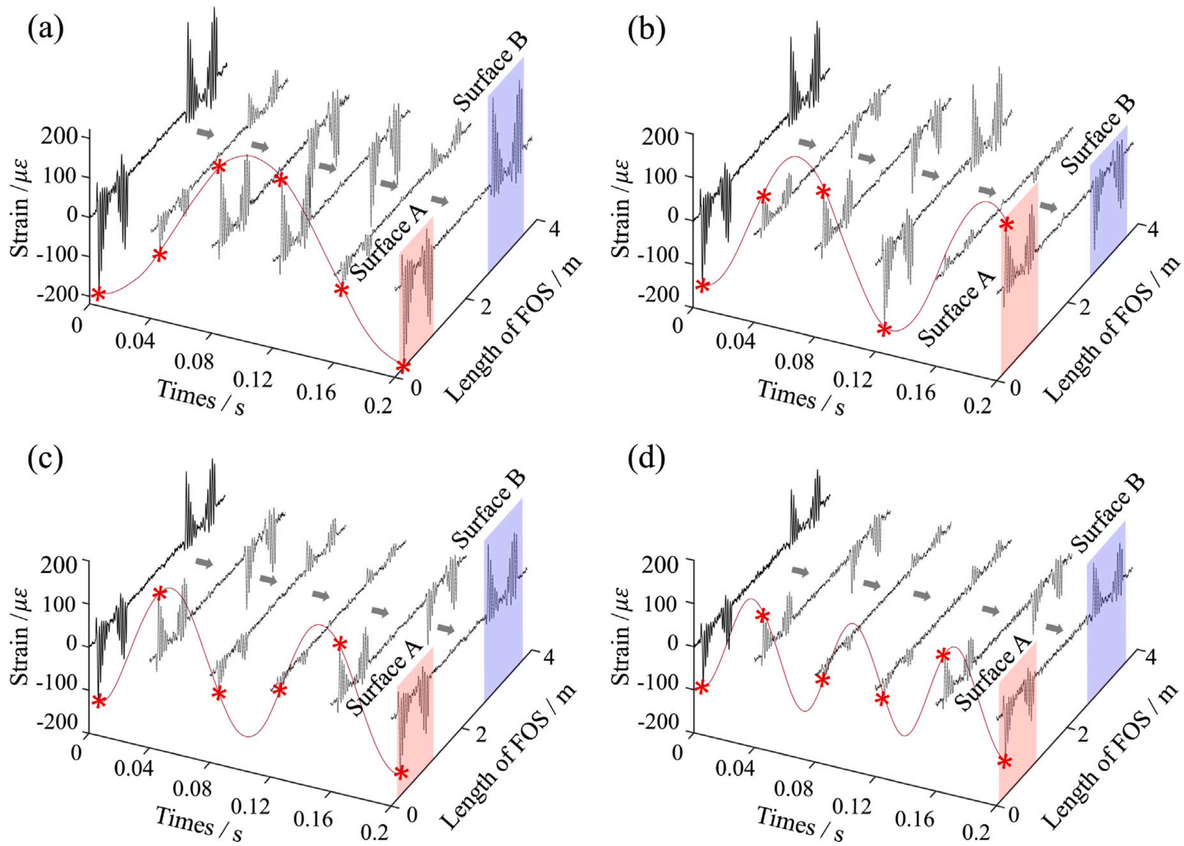

Fig. 5. The dynamic strain measurement of SMF network: (a) measurements under 5 Hz vibration load; (b) measurements under 8 Hz vibration load; (c) measurements under 10 Hz vibration load; (d) measurements under 15 Hz vibration load.

requiring customized tooling. Epoxy was selected for its ability to cure at room temperature, simplifying the installation of the complex sensor network. A schematic of this installation procedure is shown in Fig. 3(f). Additionally, "Surface A" of the specimen refers to the side attached to the shaker. Three distinct positions, with coordinates L1 (95, mm, 246, mm), L2 (50, mm, 170, mm), and L3 (35, mm, 210, mm), were selected to apply the vibration loads. The rationale for selecting these three excitation positions was to ensure spatial coverage of the specimen. Specifically, L2 is located along the centerline of the plate, representing symmetric loading; L1 is located near the right edge; and L3 is located near the left edge. In this way, the excitation points cover central and lateral regions of the specimen, allowing the validation of the deformation reconstruction under different spatial loading conditions.

The vibration generation system consists of a shaker, as shown in Fig. 3(d), with the signal captured by the Spider and Crystal Instruments Engineering Data Management (EDM) Software. During the vibration experiment, a fixed-frequency sine wave was generated by the system to serve as the excitation signal, as shown in Fig. 3(c), with the vibration direction oriented horizontally and parallel to the surface of the table. Sinusoidal excitations were deliberately chosen because they provide a controlled, repeatable, and fundamental dynamic input for structural dynamics testing, thereby allowing accurate benchmarking of the proposed deformation digital twin framework against motion capture validation. This approach is widely adopted in structural dynamics research as a preliminary step before extending to more complex excitations such as broadband or random loads [8,62,63]. To assess the generalization capability of the proposed DT framework under representative service-like conditions, four different excitation signals with frequencies of 5 Hz, 8 Hz, 10 Hz, and 15 Hz were employed. The focus on low-frequency excitations is motivated by two factors: (i) aircraft structures are predominantly subjected to low-frequency dynamic loads (e.g., gusts, turbulence, and maneuver-induced vibrations) during service [64–66], and (ii) lower frequencies induce larger deformation amplitudes, which are more suitable for evaluating shape sensing accuracy. At higher frequencies, by contrast, the shaker power limitations reduce the deformation amplitudes, thus providing a more stringent test of the framework's robustness under smaller measurable responses.

In the distributed fiber optic sensing system, a commercial OFDR system (model: ODiSI-B) manufactured by LUNA company was utilized to measure real-time strain data from the SMF network. The ODiSI-B system operates at a sampling frequency of 100 Hz. The SMF (model: SM1500 (9/125)P) manufactured by FIBRECORE company was employed in the experiments. Additionally, the optical imaging system was constructed using a Canon EOS 5D Mark II camera, which was used to capture the motion of the specimen during real-time vibration. The camera's recording frequency is 60 Hz, and the motion state of the specimen at a specific moment is shown in Fig. 3(d) as an example.

The iFEM mesh utilized in this study is illustrated in Fig. 4. The red curve in the figure represents the trace of the SMF on the surface specimen. The specimen is discretized into 32 iFEM elements, labeled sequentially as $e_1, e_2, \ldots, e_{32}$. The normal and strain data for these iFEM elements are derived from the measurements of the SMF network, based on the algorithm outlined in Section 2.2. The corresponding results are presented and discussed in the following Section 4.1.

4. Results and discussion

This section presents the experimental results and their corresponding discussions. Section 4.1 begins with a discussion of the strain data of the iFEM elements, which are calculated using the proposed algorithm (detailed in Section 2.2). Section 4.2 follows with an analysis of the shape reconstruction results based on the iFEM. The motion capture

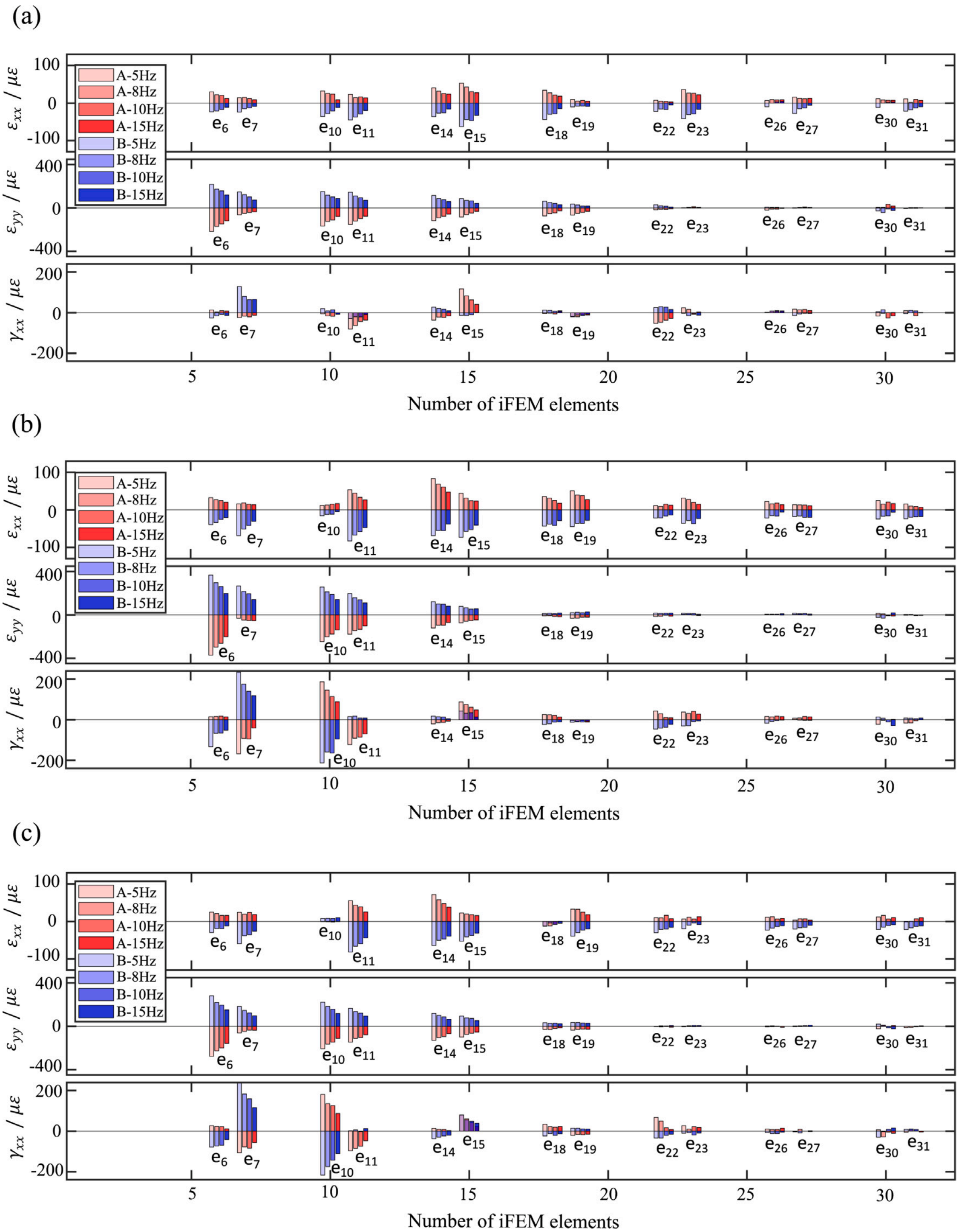

Fig. 6. The calculated strain of CFRP specimen based on proposed strain acquisition algorithm: (a) vibration load position 1; (b) vibration load position 2; (c) vibration load position 3.

results using the KLT algorithm are then discussed in Section 4.3. Lastly, an error analysis of the displacement between the shape reconstruction and motion capture results is provided.

4.1. The experiment measurements and strain acquired by proposed algorithm

Based on the experimental setup, dynamic loads with frequencies of 5 Hz, 8 Hz, 10 Hz, and 15 Hz were applied to three distinct positions on the specimen using the shaker. To demonstrate the data collected by the ODiSI-B system during the experiment, time-domain slices of the strain measurements corresponding to the loads applied at position 1 are presented in Fig. 5.

Fig. 5 presents the strain measurements under vibration loads of 5 Hz, 8 Hz, 10 Hz, and 15 Hz, respectively. Each figure displays six strain profiles over a period of 0.2 s, with measurements taken at consistent time intervals. The *z*-axis represents the measured strain values. As shown in these figures, the length of the SMF installed on the specimen exceeds 4 m. Each strain profile includes three types of strain data: measurements from Surface A (highlighted with a red translucent

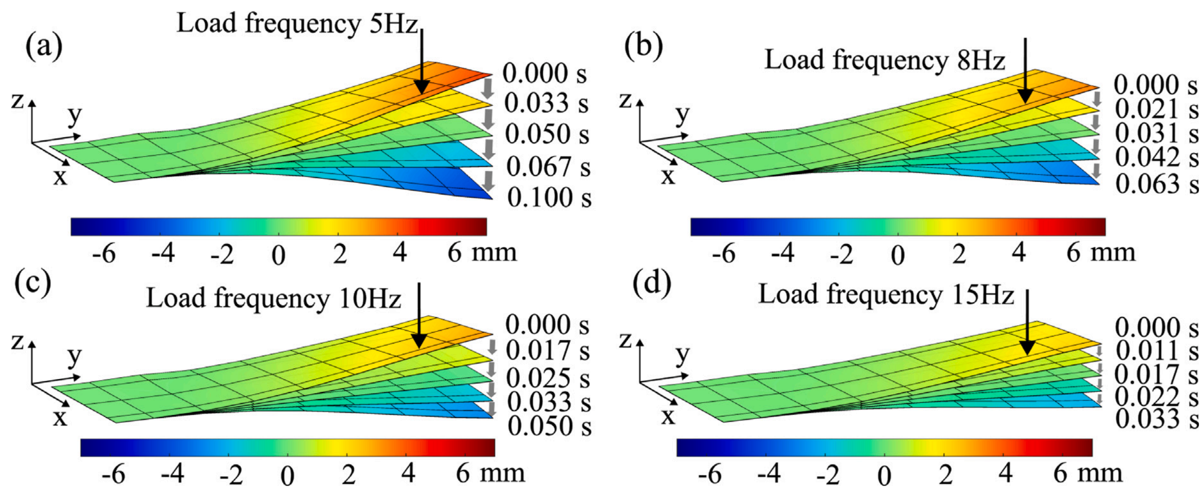

Fig. 7. The deformation reconstruction results of the CFRP specimen under vibration loads with different frequencies at position 1: (a) deformation under 5 Hz vibration load; (b) deformation under 8 Hz vibration load; (c) deformation under 10 Hz vibration load; (d) deformation under 15 Hz vibration load.

quadrilateral), measurements from Surface B (highlighted with a blue translucent quadrilateral), and vibration-free strain measurements from the unbonded sections of the SMF sensor. The red curve with stars in these figures illustrates the strain variation over time for a single measurement segment of the SMF sensor, corresponding to the applied vibrational load.

The normal and shear strains on both surfaces of the specimen are dynamically calculated using the strain calculation algorithm described in Section 2.2, based on the measurements shown in Fig. 5. An example of the calculated normal and shear strains for all iFEM elements is presented in Fig. 6. These results correspond to the condition when the load reaches its maximum value during vibration, which coincides with the peak values of the red curves shown in Fig. 5.

Fig. 6 presents the calculated strain results for vibration loads applied at positions 1, 2, and 3, respectively. The x-axis represents the serial numbers of the iFEM elements, as defined in Fig. 4, while the y-axis displays the calculated normal and shear strain values. In these bar graphs, strain results for iFEM elements on Surface A are shown in red, and those for Surface B are shown in blue. For each iFEM element, four bars of varying shades are used to compare strain calculations under vibration loads at different frequencies, with darker bars corresponding to higher-frequency vibration loads.

A comparison of the normal and shear strain results under varying vibration frequencies in Fig. 6(a) shows that strain amplitude decreases as vibration frequency increases. This indicates that the specimen undergoes less deformation during experiments conducted at higher vibration frequencies. A similar trend is observed in Fig. 6(b) and (c). This behavior can be attributed to the power limitations of the shaker: as the vibration frequency increases, the vibration amplitude decreases, leading to reduced deformation of the specimen.

4.2. The shape reconstruction results

Using the calculated normal and shear strains for all iFEM elements, as detailed in Section 4.1, the displacement field of the specimen was determined using iFEM. The resulting deformations under vibration loads applied at position 1 are shown in Fig. 7(a), (b), (c), and (d), corresponding to vibration frequencies of 5 Hz, 8 Hz, 10 Hz, and 15 Hz, respectively. These figures illustrate the motion of the specimen during a half sinusoidal vibration cycle, starting at the maximum positive load and ending at the maximum negative load along the z-axis. The specimen exhibits both bending and twisting deformations, attributed to the asymmetric loading along the z-axis. Furthermore, the deformation amplitude decreases with increasing vibration frequency, consistent with the conclusions obtained in Section 4.1.

Fig. 8 compares the shape reconstruction results for different load positions under a 5 Hz vibration load. The results for positions 1, 2, and 3 are shown in Fig. 8(a), (b), and (c), respectively. Similar to Fig. 7, these figures illustrate the motion of the specimen during a half sinusoidal vibration cycle, starting at the maximum positive load and ending at the maximum negative load. As observed, the vibration load applied at position 2 results in the largest deformation, followed by position 3. In contrast, the smallest deformation occurs when the vibration load is applied at position 1. This variation can be attributed to the differing y-axis coordinates of the load positions, with greater deformations observed when the load position is closer to the fixed edge of the specimen.

4.3. The motion capture results

The KLT-based motion capture technique is employed in this DT framework to dynamically validate the shape reconstruction results obtained via iFEM. Fig. 9 shows the displacement of the specimen on the yoz plane, as recorded by the camera, under vibration loads of 5 Hz, 8 Hz, 10 Hz, and 15 Hz applied at position 1. These results correspond to the iFEM-based findings presented in Fig. 7. Similar to Fig. 7, Fig. 9 illustrates the motion of the specimen during a half sinusoidal vibration cycle, starting at the maximum positive load and ending at the maximum negative load. Consistent with the observations in Sections 4.1 and 4.2, the results confirm that the deformation amplitude decreases as the vibration frequency increases, aligning with the trends observed in the experiments.

To mathematically characterize the motion capture results, three points are selected using the KLT algorithm to compute real-time displacements under various load conditions. These points are defined as follows: point 1 (indicated by a red cross) with coordinates (110, 110, 0), point 2 (indicated by a blue cross) with coordinates (110, y_{load}, 0), and point 3 (indicated by a yellow cross) with coordinates (110, 300, 0). The variable y_{load} in the coordinates of point 2 corresponds to the y-axis positions of load position 1, position 2, and position 3, which are 246 mm, 170 mm, and 210 mm, respectively.

The displacements of point 1, point 2, and point 3 are presented in Fig. 10. The x-axis represents time over a duration of 1 s, while the y-axis indicates the displacements measured using the KLT-based motion capture technique. At a 5 Hz vibration load, the points exhibit their largest displacements, as shown in Fig. 10(a), with amplitudes reaching approximately ±0.7 mm, ±3.5 mm, and ±4.5 mm for point 1, point 2, and point 3, respectively. In contrast, under a 15 Hz vibration load, the displacements are significantly smaller, as demonstrated in Fig. 10(d),

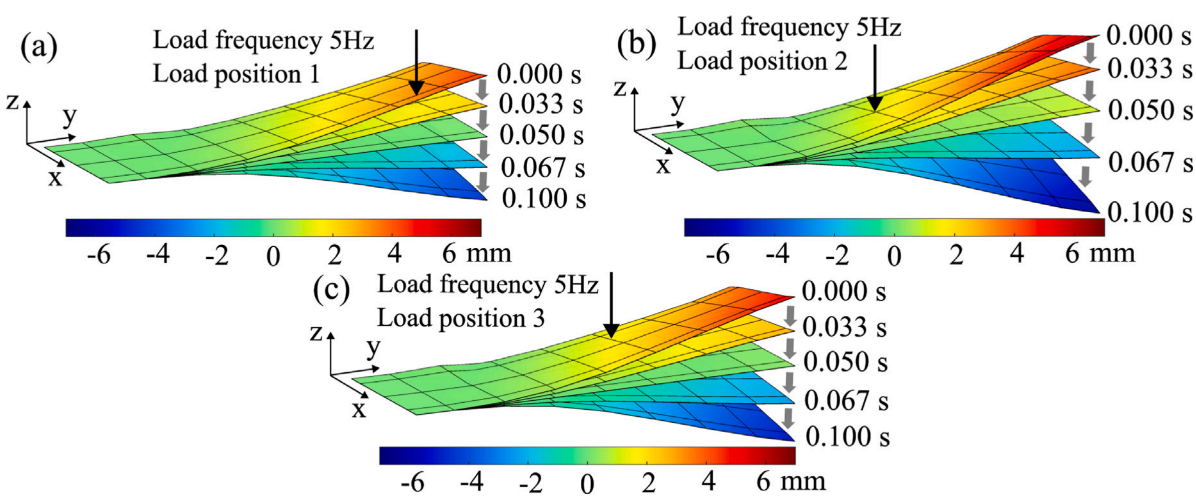

Fig. 8. The deformation reconstruction results of the CFRP specimen under 5 Hz vibration loads at different load positions: (a) deformation under load position 1; (b) deformation under load position 2; (c) deformation under load position 3.

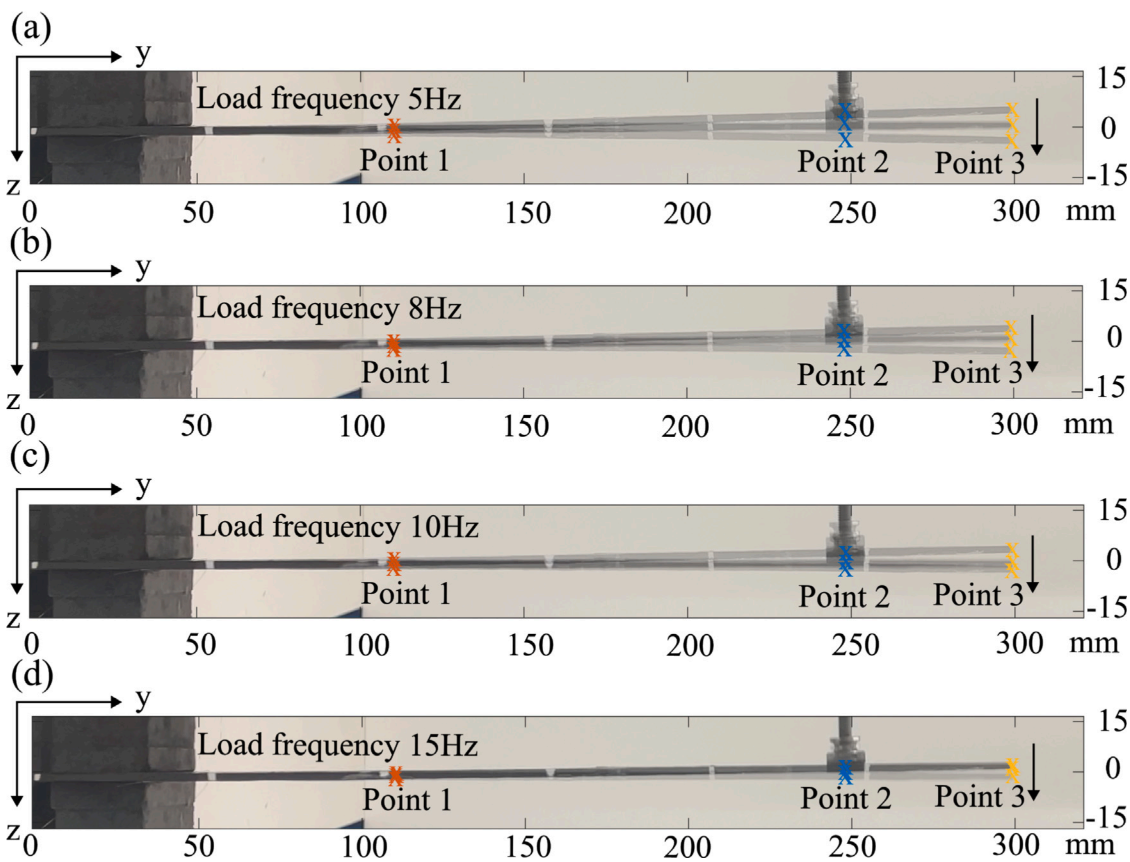

Fig. 9. The dynamic behavior of the CFRP specimen when vibration loads with different frequencies are applied to position 1: (a) deformation under 5 Hz vibration load; (b) deformation under 8 Hz vibration load; (c) deformation under 10 Hz vibration load; (d) deformation under 15 Hz vibration load.

with values of approximately, ±0.4 mm, ±1.8 mm, and, ±2.3 mm for point 1, point 2, and point 3, respectively.

To compare the results across different loading positions, Fig. 11 illustrates the dynamic behavior of the specimen on the *yoz* plane under a 5 Hz vibration load applied at position 1, position 2, and position 3. Consistent with the findings from Figs. 6 and 8, it is clear that the specimen experiences greater deformation as the *y*-axis coordinates of the load position move closer to 0, or the fixed edge.

The motion capture results for the three points shown in Fig. 11 are quantitatively presented in Fig. 12. Panels (a), (b), and (c) display the results for vibration loads applied to position 1, position 2, and position 3, respectively. The *y*-axis coordinate of load position 2 is the smallest (see Section 3), leading to the greatest deformation. For example, the displacements of point 1, point 2, and point 3 in Fig. 12(b) reach ±1.1 mm, ±2.9 mm, and ±6.4 mm, respectively. In comparison, the displacements for load position 1, shown in Fig. 12(a), are only

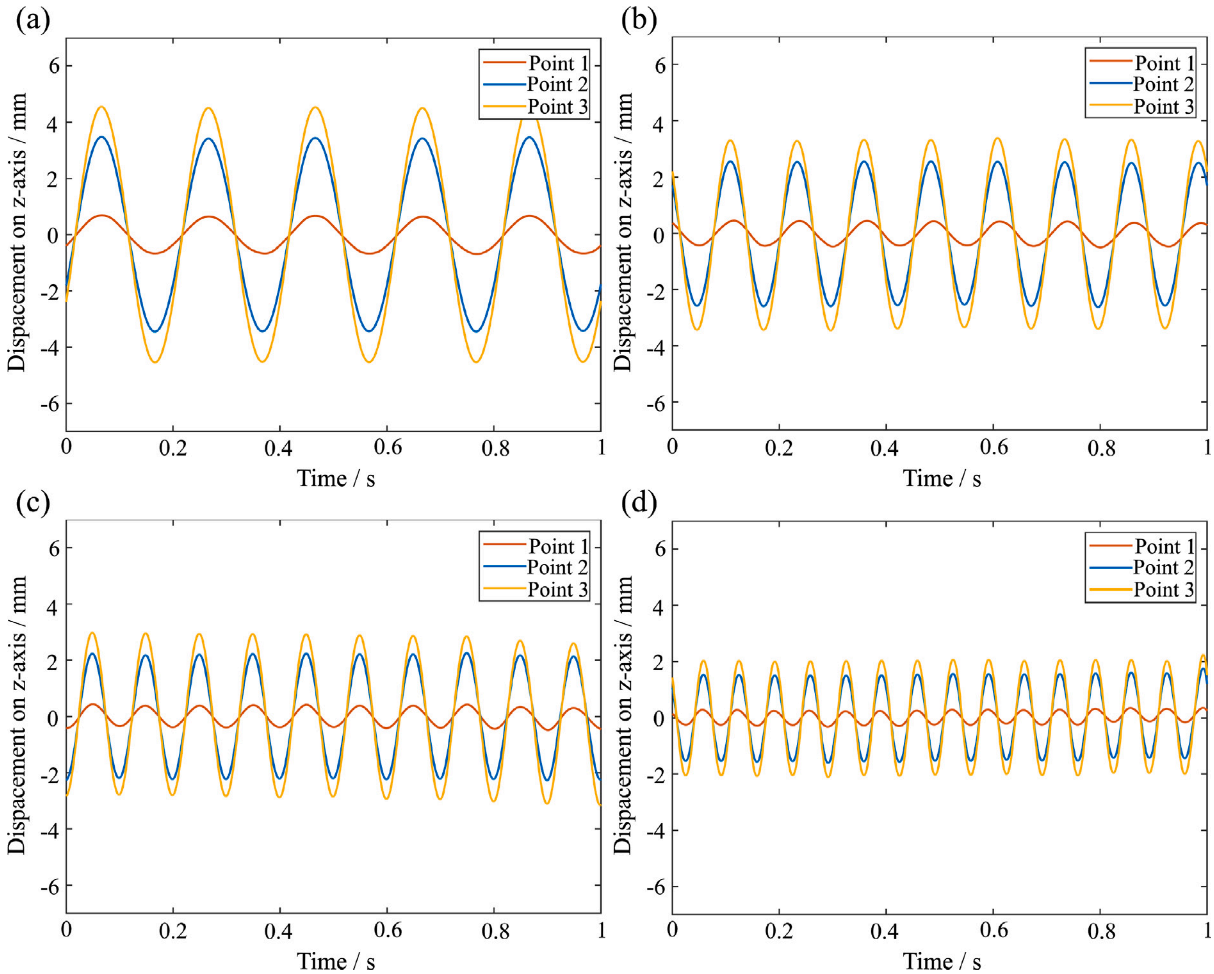

Fig. 10. The displacement of point 1, 2, and 3 obtained by KLT-based motion capture under different vibration frequencies when load is applied to position 1: (a) 5 Hz; (b) 8 Hz; (c) 10 Hz; (d) 15 Hz.

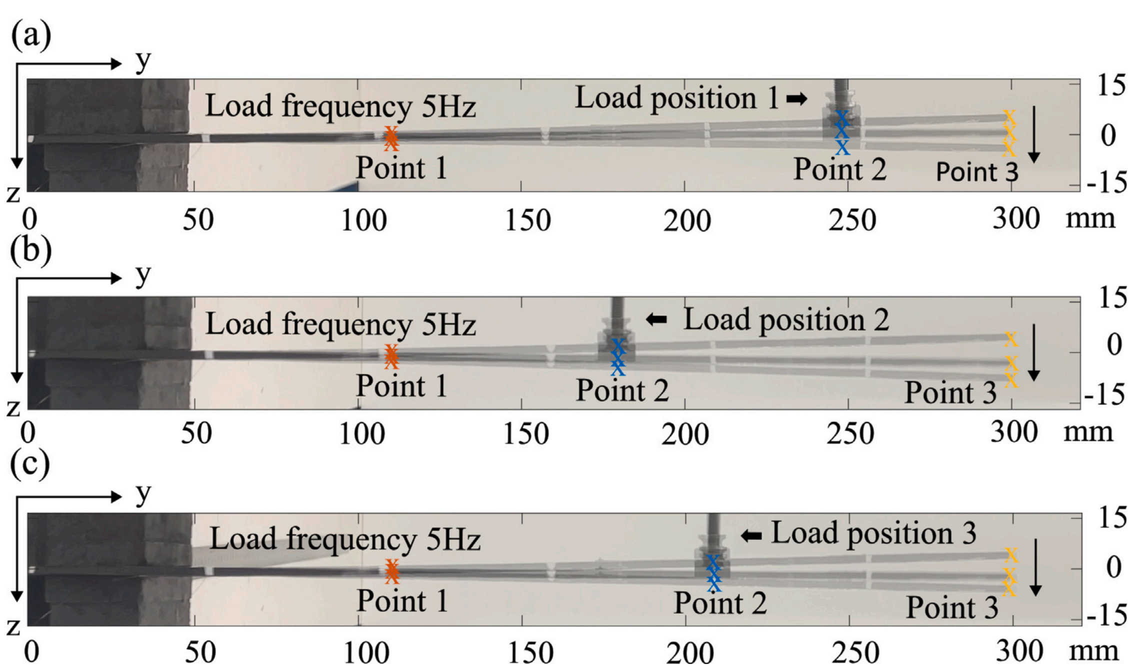

Fig. 11. The dynamic behavior of the CFRP specimen when 5 Hz vibration load is applied to various positions: (a) deformation under load position 1; (b) deformation under load position 2; (c) deformation under load position 3.

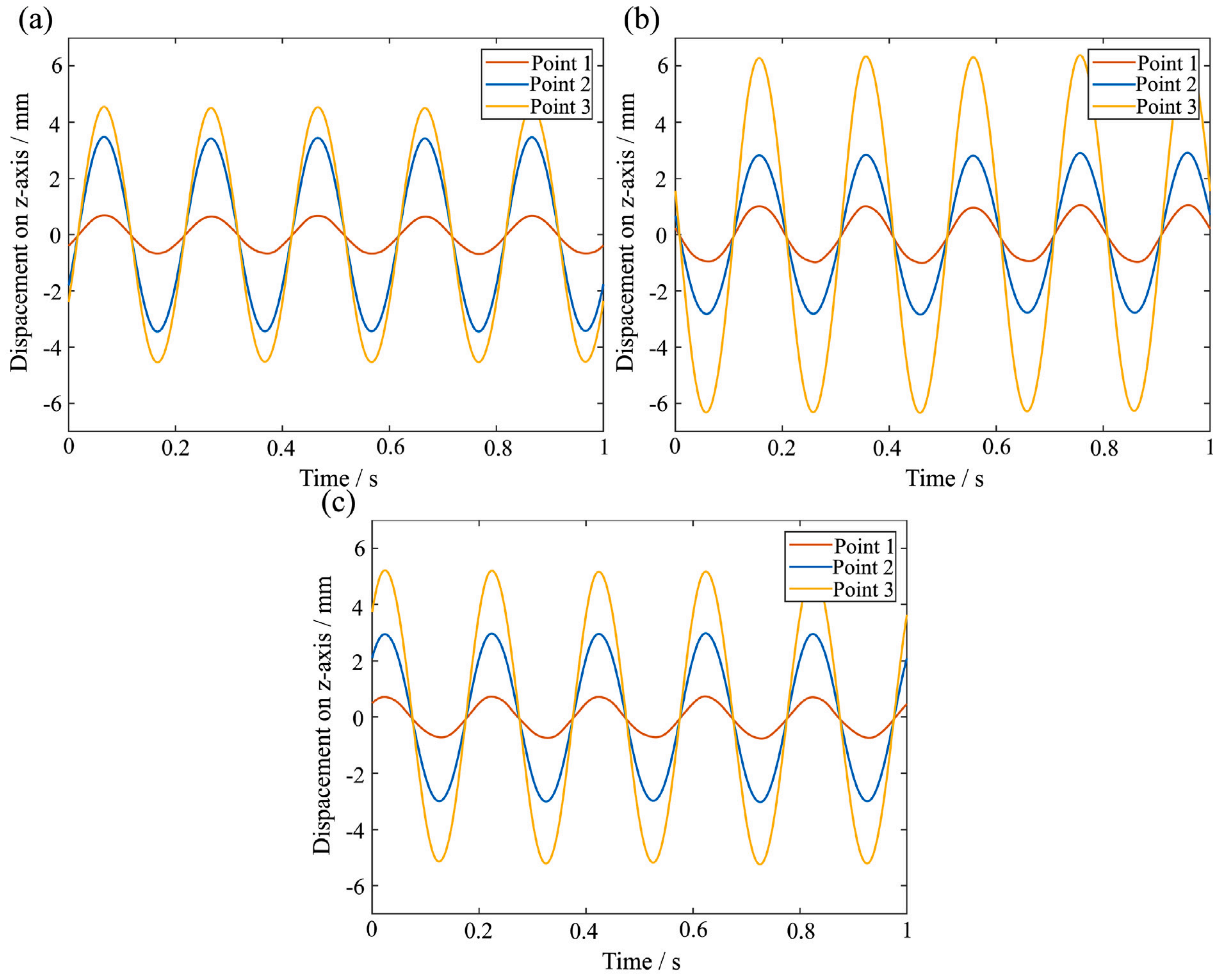

Fig. 12. The displacement of points 1, 2, and 3 obtained by KLT-based motion capture when 5 Hz vibration loads are applied to positions 1, 2, and 3: (a) load position 1; (b) load position 2; (c) load position 3.

±0.7 mm, ±3.5 mm, and ±4.5 mm, respectively. These results align closely with the shape reconstruction outcomes presented in Fig. 8.

Summarizing the results presented in Sections 4.2 and 4.3, two important conclusions can be drawn from the experiments. First, the deformation amplitude decreases with increasing load frequency, a trend consistently observed in both shape reconstruction and motion capture results. Second, the vibration load applied at position 2 produces the largest deformation, followed by positions 3 and 1, again confirmed by both measurement approaches. For clarity and completeness, a comparative visual summary has been provided in the supplementary material. This summary consolidates all deformation reconstruction and motion capture results, allowing direct comparison of deformation trends across different frequencies and loading positions.

4.4. The error analysis of deformation reconstruction

Based on the previous analysis, it can be concluded that the shape reconstruction using iFEM aligns well with the displacement measurements obtained through KLT-based motion capture. This subsection provides a detailed evaluation of the errors between the shape reconstruction and motion capture results. Specifically, a comparison is made between the displacements measured by motion capture and those obtained through shape reconstruction for point 1, point 2, and point 3. Since the experimental loads follow a regular sinusoidal pattern, the displacement results at the maximum and minimum states of the sinusoidal amplitude are used to assess the accuracy of the reconstructed displacement field. As shown in Fig. 13, the x-axis represents the frequency of vibration loads, while the y-axis indicates the maximum displacement along the z-axis (in both positive and negative directions) during the experiments. Specifically, Fig. 13(a), (b), and (c) present the results for point 1 (as defined in Fig. 11) under vibration loads applied at position 1, position 2, and position 3, respectively. Fig. 13(d), (e), and (f) display the corresponding results for point 2, while the final three subfigures show the corresponding results for point 3.

A comparison of the results shown in Fig. 13(g), (h), and (i) reveals that the specimen undergoes the greatest deformation when vibration loads are applied at position 2. Additionally, the observation that deformation decreases as vibration frequency increases holds true across all subfigures in Fig. 13. These findings are consistent with the analysis presented in earlier subsections. Notably, the results in Fig. 13 show that the displacement measurements obtained from both motion capture and shape reconstruction exhibit errors smaller than 0.3 mm. This indicates that the proposed DT framework achieves highly accurate dynamic deformation reconstruction, which can be validated in real-time.

It is important to note that only the displacements of three points obtained through motion capture are used in this study to validate the shape reconstruction results. This is because the proposed DT framework is designed to provide a low-cost, flexible, and easily implementable solution for dynamic validation of shape reconstruction, rather than for validating full-field displacement. In practical applications, the number and positions of the points to be captured can be adjusted based on factors such as structural complexity or the

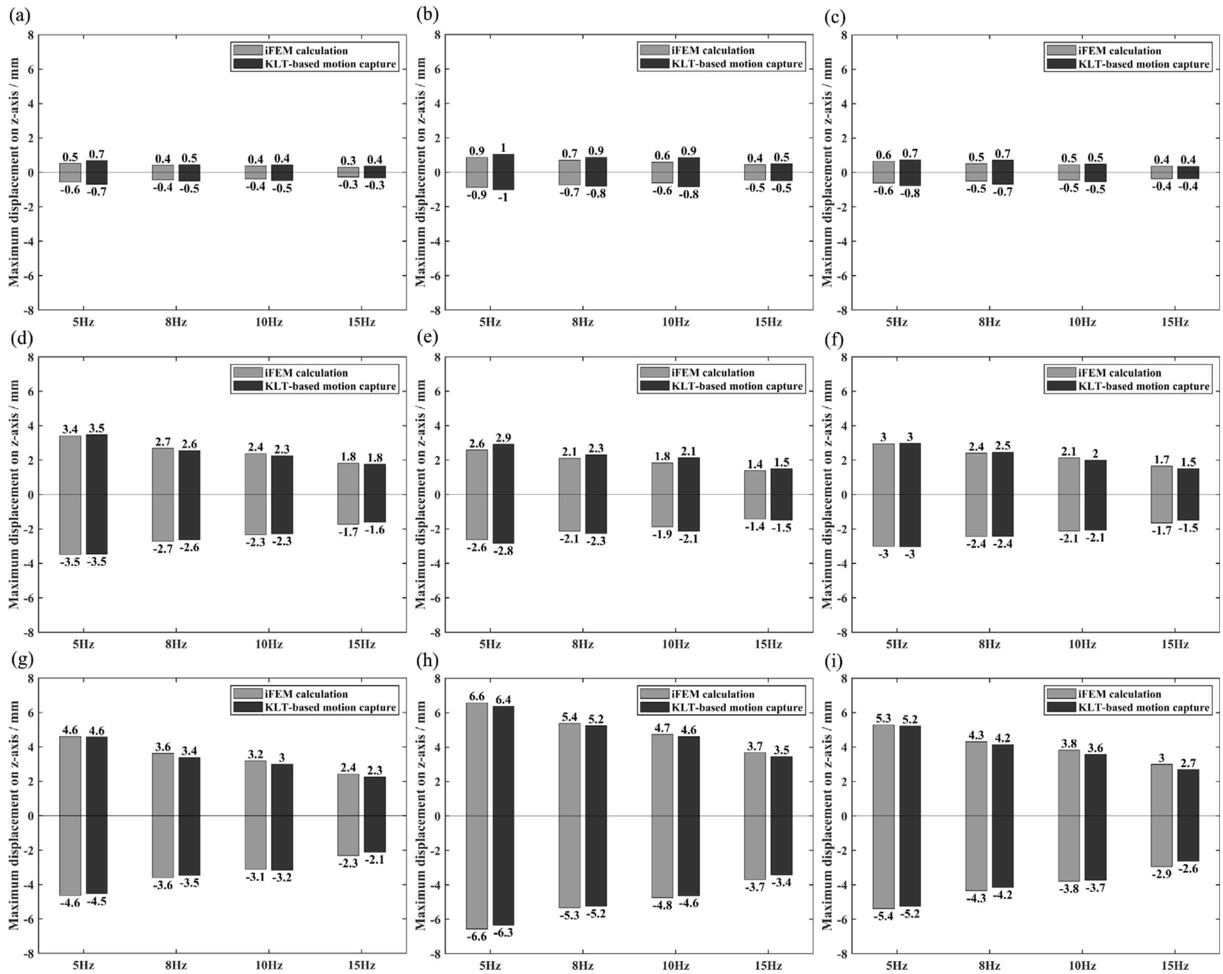

Fig. 13. Comparison of displacement results for points 1, 2, and 3 obtained using iFEM and KLT-based motion capture, under different load positions and vibration frequencies: (a) point 1 and load position 1; (b) point 1 and load position 2; (c) point 1 and load position 3; (d) point 2 and load position 1; (e) point 2 and load position 2; (f) point 2 and load position 3; (g) point 3 and load position 1; (h) point 3 and load position 2; (i) point 3 and load position 3.

configuration of the optical imaging system. Moreover, in the KLT-based motion capture algorithm, the points to be tracked need to be defined only once during the system initialization phase of the proposed DT framework.

5. Conclusions

To address challenges in dynamic shape reconstruction using iFEM — such as time-synchronized data acquisition, EOVs, and dynamic validation and calibration — a deformation DT framework is proposed in this paper. The core components of the proposed framework include a real-time strain acquisition scheme, dynamic shape sensing based on iFEM, and a dynamic validation and calibration mechanism. The strain acquisition scheme is based on distributed fiber optic sensing and the strain rosette principle.

The proposed framework leverages the digital representation of the SMF network, which provides the capability to accommodate diverse EOVs, such as modifications to the iFEM mesh, sensor layout, or adaptation to harsh environments, while preserving time-synchronized strain acquisition. To validate the proposed DT framework and assess its effectiveness, experimental investigations were conducted on a composite laminate specimen subjected to sinusoidal vibration loads of varying frequencies (5 Hz, 8 Hz, 10 Hz, and 15 Hz), applied at three distinct locations on the specimen. Results demonstrated the framework's high accuracy, achieving a maximum shape reconstruction error of only 0.3 mm compared to motion capture results. These findings demonstrate the framework's ability to handle dynamic loading conditions and spatial variations with high accuracy.

In conclusion, the proposed deformation DT framework provides a robust and efficient solution for dynamic shape reconstruction, demonstrating strong potential for applications in aerospace, SMF monitoring, and other engineering domains where precise shape sensing under EOVs is critical. Consistent with established practices in the literature, the present study validates the framework under controlled sinusoidal excitations across multiple frequencies and loading positions, thereby confirming its effectiveness for dynamic conditions. Future work will aim to broaden the scope of validation by extending the framework to more diverse materials and complex loading scenarios, including random vibrations, transient impacts, and multi-directional excitations. In addition, further investigations will focus on mitigating sources of error, such as sensor precision, iFEM modeling assumptions, and experimental boundary conditions, to enhance the robustness, scalability, and reliability of the framework in real-world applications, such as aerospace vehicles, wind turbines, civil infrastructure, and HDT systems.

CRediT authorship contribution statement

Yingwu Li: Writing – original draft, Validation, Data curation, Conceptualization. **Yuhang Pan:** Writing – original draft, Visualization, Validation, Data curation. **Zahra Sharif-Khodaei:** Writing – review & editing, Supervision, Resources, Funding acquisition.

Declaration of competing interest

The authors declare that they have no known competing financial interests or personal relationships that could have appeared to influence the work reported in this paper.

Acknowledgments

The authors would like to express their gratitude to the President's Scholarship at Imperial College London and the Great Britain China Educational Trust for funding Yingwu Li's research. Additionally, this work was partially supported by UKRI under the UK Government's Horizon Europe Guarantee (under grant agreement No 101096073, AVATAR project).

Data availability

Data will be made available on request.

References

[1] M. Freydin, M.K. Rattner, D.E. Raveh, I. Kressel, R. Davidi, M. Tur, Fiber-optics-based aeroelastic shape sensing, AIAA J. 57 (12) (2019) 5094–5103.
[2] V. Biazi, L. Avellar, A. Frizera, A. Leal-Junior, Influence of two-plane position and stress on intensity-variation-based sensors: Towards shape sensing in polymer optical fibers, Sensors 21 (23) (2021) 7848.
[3] M. Elkington, E. Almas, B. Ward-Cherrier, N. Pestell, J. Lloyd, C. Ward, N. Lepora, Real time defect detection during composite layup via tactile shape sensing, Sci. Eng. Compos. Mater. 28 (1) (2021) 1–10.
[4] C.M. Monsberger, W. Lienhart, Distributed fiber optic shape sensing of concrete structures, Sensors 21 (18) (2021) 6098.
[5] B. Cheng, W. Zhu, J. Liu, L. Yuan, H. Xiao, 3D beam shape estimation based on distributed coaxial cable interferometric sensor, Smart Mater. Struct. 26 (3) (2017) 035017.
[6] H. Wu, L. Liang, H. Wang, S. Dai, Q. Xu, R. Dong, Design and measurement of a dual FBG high-precision shape sensor for wing shape reconstruction, Sensors 22 (1) (2021) 168.
[7] J. Xu, X. Zhou, M. Giglio, C. Sbarufatti, L. Dong, Variational neural network embedded with digital twins for probabilistic structural damage quantification, AIAA J. 63 (6) (2025) 2474–2486.
[8] A. Kefal, E. Oterkus, A. Tessler, J.L. Spangler, A quadrilateral inverse-shell element with drilling degrees of freedom for shape sensing and structural health monitoring, Eng. Sci. Technol. an Int. J. 19 (3) (2016) 1299–1313.
[9] D.A. Maisano, L. Mastrogiacomo, F. Franceschini, S. Capizzi, G. Pischedda, D. Laurenza, G. Gomiero, G. Manca, Dimensional measurements in the shipbuilding industry: on-site comparison of a state-of-the-art laser tracker, total station and laser scanner, Prod. Eng. 17 (3) (2023) 625–642.
[10] K. Kim, H. Sohn, Dynamic displacement estimation by fusing LDV and LiDAR measurements via smoothing based Kalman filtering, Mech. Syst. Signal Process. 82 (2017) 339–355.
[11] R. Yang, Y. Li, D. Zeng, P. Guo, Deep DIC: Deep learning-based digital image correlation for end-to-end displacement and strain measurement, J. Mater. Process. Technol. 302 (2022) 117474.
[12] H. Wu, H.-H. Zhu, C.-C. Zhang, G.-Y. Zhou, B. Zhu, W. Zhang, M. Azarafza, Strain integration-based soil shear displacement measurement using high-resolution strain sensing technology, Measurement 166 (2020) 108210.
[13] A. Sun, Z. Wu, D. Fang, J. Zhang, W. Wang, Multimode interference-based fiber-optic ultrasonic sensor for non-contact displacement measurement, IEEE Sensors J. 16 (14) (2016) 5632–5635.
[14] T.Q. Thai, X. Zhuang, T. Rabczuk, A nonlinear geometric couple stress based strain gradient Kirchhoff–Love shell formulation for microscale thin-wall structures, Int. J. Mech. Sci. 196 (2021) 106272.
[15] A.J. Sadowski, J.M. Rotter, Solid or shell finite elements to model thick cylindrical tubes and shells under global bending, Int. J. Mech. Sci. 74 (2013) 143–153.
[16] S. He, Y. Wang, Z. Zhang, F. Xiao, S. Zuo, Y. Zhou, X. Cai, X. Jin, Interpretable machine learning workflow for evaluation of the transformation temperatures of TiZrHfNiCoCu high entropy shape memory alloys, Mater. Des. 225 (2023) 111513.
[17] M. Gherlone, P. Cerracchio, M. Mattone, Shape sensing methods: Review and experimental comparison on a wing-shaped plate, Prog. Aerosp. Sci. 99 (2018) 14–26.
[18] W.L. Ko, W.L. Richards, V.T. Tran, Displacement Theories for In-Flight Deformed Shape Predictions of Aerospace Structures, Technical Report NASA/TP-2007-214612, NASA Dryden Flight Research Center, 2007, URL: https://ntrs.nasa.gov/api/citations/20070032936/downloads/20070032936.pdf.
[19] M. Esposito, M. Gherlone, P. Marzocca, External loads identification and shape sensing on an aluminum wing box: An integrated approach, Aerosp. Sci. Technol. 114 (2021) 106743.
[20] L. Zhou, G. Yan, J. Ou, Response surface method based on radial basis functions for modeling large-scale structures in model updating, Computer-Aided Civ. Infrastruct. Eng. 28 (3) (2013) 210–226.
[21] C. Shi, X. Luo, P. Qi, T. Li, S. Song, Z. Najdovski, T. Fukuda, H. Ren, Shape sensing techniques for continuum robots in minimally invasive surgery: A survey, IEEE Trans. Biomed. Eng. 64 (8) (2016) 1665–1678.
[22] A. Kefal, I.E. Tabrizi, M. Yildiz, A. Tessler, A smoothed iFEM approach for efficient shape-sensing applications: Numerical and experimental validation on composite structures, Mech. Syst. Signal Process. 152 (2021) 107486.
[23] M.A. Abdollahzadeh, A. Kefal, M. Yildiz, A comparative and review study on shape and stress sensing of flat/curved shell geometries using C0-continuous family of iFEM elements, Sensors 20 (14) (2020) 3808.
[24] M. Gherlone, P. Cerracchio, M. Mattone, M. Di Sciuva, A. Tessler, Shape sensing of 3D frame structures using an inverse finite element method, Int. J. Solids Struct. 49 (22) (2012) 3100–3112.
[25] L. Colombo, D. Oboe, C. Sbarufatti, F. Cadini, S. Russo, M. Giglio, Shape sensing and damage identification with iFEM on a composite structure subjected to impact damage and non-trivial boundary conditions, Mech. Syst. Signal Process. 148 (2021) 107163.
[26] A. Tessler, J.L. Spangler, A least-squares variational method for full-field reconstruction of elastic deformations in shear-deformable plates and shells, Comput. Methods Appl. Mech. Engrg. 194 (2–5) (2005) 327–339.
[27] A. Kefal, E. Oterkus, Displacement and stress monitoring of a panamax containership using inverse finite element method, Ocean Eng. 119 (2016) 16–29.
[28] A. Albanesi, V. Fachinotti, I. Peralta, B. Storti, C. Gebhardt, Application of the inverse finite element method to design wind turbine blades, Compos. Struct. 161 (2017) 160–172.
[29] M. Li, A. Kefal, E. Oterkus, S. Oterkus, Structural health monitoring of an offshore wind turbine tower using iFEM methodology, Ocean Eng. 204 (2020) 107291.
[30] H. Zhu, Z. Du, Y. Tang, Automatic free span assessment for subsea pipelines using static strain data, Ocean Eng. 263 (2022) 112413.
[31] F. Zhao, A. Kefal, H. Bao, Nonlinear deformation monitoring of elastic beams based on isogeometric iFEM approach, Int. J. Non-Linear Mech. 147 (2022) 104229.
[32] P. Savino, F. Tondolo, A new approach for displacement and stress monitoring of tunnel based on iFEM methodology, Smart Mater. Struct. 31 (1) (2021) 015013.
[33] R. Roy, A. Tessler, C. Surace, M. Gherlone, Efficient shape sensing of plate structures using the inverse finite element method aided by strain pre-extrapolation, Thin-Walled Struct. 180 (2022) 109798.
[34] Y. Pan, Z.S. Khodaei, M.H.F. Aliabadi, A robust hybrid method for damage detection under varying environmental conditions, Struct. Heal. Monit. (2024) 1–16, http://dx.doi.org/10.1177/14759217241303072.
[35] F. Tao, H. Zhang, A. Liu, A.Y. Nee, Digital twin in industry: State-of-the-art, IEEE Trans. Ind. Informatics 15 (4) (2018) 2405–2415.
[36] Y. Liu, F. Dai, A review of experimental and theoretical research on the deformation and failure behavior of rocks subjected to cyclic loading, J. Rock Mech. Geotech. Eng. 13 (5) (2021) 1203–1230.
[37] M.W. Grieves, Digital twins: past, present, and future, in: The Digital Twin, Springer, 2023, pp. 97–121.
[38] X. Zhou, S. He, L. Dong, S.N. Atluri, Real-time prediction of probabilistic crack growth with a helicopter component digital twin, AIAA J. 60 (4) (2022) 2555–2567.
[39] P. Wei, C. Li, Z. Jiang, D. Wang, Real-time digital twin of ship structure deformation field based on the inverse finite element method, J. Mar. Sci. Eng. 12 (2) (2024) 257.
[40] Y. Pan, Z.S. Khodaei, F. Aliabadi, Online fatigue crack detection and growth modelling through higher harmonic analysis: A baseline-free approach, Mech. Syst. Signal Process. 224 (2025) 112167.
[41] I.N. Giannakeas, Z.S. Khodaei, M. Aliabadi, Digital clone testing platform for the assessment of SHM systems under uncertainty, Mech. Syst. Signal Process. 163 (2022) 108150.
[42] X. Zhou, L. Dong, M. Dziendzikowski, K. Dragan, M. Giglio, C. Sbarufatti, Real-time in-service load tracking toward airframe digital twins, AIAA J. (2025) http://dx.doi.org/10.2514/1.J064671.
[43] C. Lo, C. Chen, R.Y. Zhong, A review of digital twin in product design and development, Adv. Eng. Informatics 48 (2021) 101297, http://dx.doi.org/10.1016/j.aei.2021.101297.
[44] J. Leng, P. Jiang, K. Xu, Q. Liu, J. Zhao, W. Bian, Digital twins-based smart manufacturing system design in Industry 4.0: A review, J. Manuf. Syst. 57 (2020) 396–415, http://dx.doi.org/10.1016/j.jmsy.2021.05.011.
[45] J. Leng, M. Zhou, Y. Xiao, H. Zhang, Q. Liu, W. Shen, Q. Su, L. Li, Digital twins-based remote semi-physical commissioning of flow-type smart manufacturing systems, J. Clean. Prod. 306 (2021) 127278, http://dx.doi.org/10.1016/j.jclepro.2021.127278.
[46] M. Fujikubo, T. Okada, H. Murayama, H. Houtani, N. Osawa, K. Iijima, K. Hamada, K. Toh, M. Oka, S. Hirakawa, et al., A digital twin for ship structures—R&D project in Japan, Data-Centric Eng. 5 (2024) e7.

[47] G. Delo, R. Roy, K. Worden, C. Surace, Using the inverse finite-element method to harmonise classical modal analysis with fibre-optic strain data for robust population-based structural health monitoring, Strain 61 (1) (2025) e12481.
[48] J. Chen, Y. Shi, C. Yi, H. Du, J. Kang, D. Niyato, Generative-AI-driven human digital twin in IoT healthcare: A comprehensive survey, IEEE Internet Things J. 11 (2024) 34749–34773, http://dx.doi.org/10.1109/JIOT.2024.3421918.
[49] S. Okegbile, J. Cai, H. Zheng, J. Chen, C. Yi, Differentially private federated multi-task learning framework for enhancing human-to-virtual connectivity in human digital twin, IEEE J. Sel. Areas Commun. 41 (2023) 3533–3547, http://dx.doi.org/10.1109/JSAC.2023.3310106.
[50] J. Chen, C. Yi, S. Okegbile, J. Cai, X. Shen, Networking architecture and key supporting technologies for human digital twin in personalized healthcare: A comprehensive survey, IEEE Commun. Surv. Tutorials 26 (2024) 706–746, http://dx.doi.org/10.1109/COMST.2023.3308717.
[51] F.J.G. de Oliveira, Z.S. Khodaei, O.R.H. Buxton, Simultaneous measurement of the distributed longitudinal strain and velocity field for a cantilevered cylinder exposed to turbulent cross flow, Exp. Fluids 65 (134) (2024).
[52] F. Zhao, X. Zhou, S. He, C. Wang, L. Dong, S.N. Atluri, B-Spline surface-based reduced-order modeling of nonplanar crack growth in structural digital twins, AIAA J. 62 (1) (2024) 360–373.
[53] P.F. Díaz-Maroto, A. Fernández-López, J. García-Alonso, M. Iglesias, A. Güemes, Buckling detection of an omega-stiffened aircraft composite panel using distributed fibre optic sensors, Thin-Walled Struct. 132 (2018) 375–384.
[54] Y. Li, Z. Sharif-Khodaei, A novel damage detection method for carbon fibre reinforced polymer structures based on distributed strain measurements with fibre optical sensor, Mech. Syst. Signal Process. 208 (2024) 110954.
[55] Y. Li, Z. Sharif-Khodaei, Accuracy of distributed strain sensing with single-mode fibre in composite laminates under thermal and vibration loads, Struct. Control. Heal. Monit. 2023 (1) (2023) 9269987.
[56] Y.-s. Kwon, K. Naeem, M.Y. Jeon, I.-B. Kwon, Enhanced sensitivity of distributed-temperature sensor with Al-coated fiber based on OFDR, Opt. Fiber Technol. 48 (2019) 229–234.
[57] M.M. Wharton, Photogrammetry and mean intensity mapping as methods of low-cost structural health monitoring, Mech. Syst. Signal Process. 219 (2024) 111583.
[58] D. Tan, J. Li, H. Hao, Target-free vision method for planar displacement measurement of structures subjected to out-of-plane movement by UAV, J. Sound Vib. 600 (2025) 118873.
[59] K. Zhou, M.-G. Duan, Z.-L. Wu, L.-H. Zhi, F. Hu, Dynamic behavior monitoring of twin supertall buildings during super typhoon soksuri using social sensing data, J. Build. Eng. 95 (2024) 110119.
[60] B.D. Lucas, T. Kanade, An iterative image registration technique with an application to stereo vision, in: IJCAI'81: 7th International Joint Conference on Artificial Intelligence, Vol. 2, 1981, pp. 674–679.
[61] Y. Li, Z. Sharif-Khodaei, Shape sensing of composite shell using distributed fibre optic sensing, Int. J. Mech. Sci. 286 (2025) 109859.
[62] Y. Wang, H. Li, Dynamics-guided support vector machines for response analysis of steel frame under Sine wave excitation, Buildings 15 (9) (2025) 1399, http://dx.doi.org/10.3390/buildings15091399.
[63] C.-D. Bratu, I.-C. Oncescu, I. Dima, A. Petre, The validation of an aerospace structure through the sine vibration analysis, INCAS Bull. 10 (2) (2018) 145–156, http://dx.doi.org/10.13111/2066-8201.2018.10.2.14.
[64] D. Ali, A. Shahzad, T. Khan, Development of fatigue loading spectra from flight test data, Procedia Struct. Integr. 2 (2016) 3296–3304, http://dx.doi.org/10.1016/j.prostr.2016.06.411.
[65] Development of fatigue loading spectra, in: ASTM Special Technical Publication STP 1006, ASTM, 1989, http://dx.doi.org/10.1520/STP1006-EB.
[66] V. Gallagher, R. York, H. Fuchs, J. Potter, R. Watanabe, Fatigue spectra development for airborne stores, in: Development of Fatigue Loading Spectra, ASTM STP 1006, ASTM, 1989, URL: www.astm.org.